Spin transport in tantalum studied using magnetic single and double layers

Eric Montoya,[1,*] Pavlo Omelchenko,[1,†] Chris Coutts,[1] Nicholas R. Lee-Hone,[1] René Hübner,[2] David Broun,[1,3] Bret Heinrich,[1] and Erol Girt[1,‡]

[1]*Department of Physics, Simon Fraser University, 8888 University Dr, Burnaby, BC, Canada V5A 1S6*

[2]*Institute of Ion Beam Physics and Materials Research, Helmholtz-Zentrum Dresden-Rossendorf, Dresden, Germany*

[3]*Canadian Institute for Advanced Research, Toronto, Ontario, Canada M5G 1Z8*

(Received 13 May 2016; published 12 August 2016)

We report on spin transport in sputter-grown Ta films measured by ferromagnetic resonance. Spin diffusion length and spin mixing conductance are determined from magnetic damping measurements for a varying thickness of Ta layer $0 \leqslant d_{\mathrm{Ta}} \leqslant 10$ nm. The different boundary conditions of single- and double-magnetic-layer heterostructures Py|Ta and Py|Ta|[Py|Fe] allow us to significantly narrow down the parameter space and test various models. We show that a common approach of using bulk resistivity value in the analysis yields inconsistent spin diffusion length and spin mixing conductance values for magnetic single- and double-layer structures. X-ray diffraction shows that bulk Ta is a combination of β-Ta and bcc-Ta. However, in the region of significant spin transport, $\lesssim 2$ nm, there is an intermediate region of growth where the Ta lacks long-range structural order, as observed by transmission electron microscopy. Thickness-dependent resistivity measurements confirm that the bulk and intermediate regions have significantly different resistivity values. We find that the data can be well represented if the intermediate region resistivity value is used in the analysis. Additionally, the data can be fit if resistivity has the measured thickness dependence and spin diffusion length is restricted to be inversely proportional to resistivity. Finally, we rule out a model in which spin diffusion length is a constant, while the resistivity has the measured thickness dependence.

DOI: 10.1103/PhysRevB.94.054416

I. INTRODUCTION

In spintronics, the electron spin is used to encode information and spin current is then used to transmit information. Technology based on spintronics has the potential to have higher processing speed and lower power consumption [1–4]. Key aspects in spintronics are understanding the generation of spin currents and transport of spin current through a device. A powerful technique to study generation and propagation of spin current is spin pumping by means of ferromagnetic resonance (FMR) [5–12]. Spin pumping is the process in which magnetization dynamics in a ferromagnet (FM) drives a nonequilibrium spin accumulation into an adjacent nonmagnetic metal (NM) [13,14].

In nonmagnetic metals (NM) with low electrical resistivity and large spin diffusion length, i.e., Cu, Al, Ag, Au (35–600 nm) [15–18], the spin pumping and spin current transport are well understood [19]. Metals with large spin-orbit coupling (Ta, Pd, Pt) [20–22] have significantly shorter diffusion lengths (1–10 nm), requiring thin samples for spin transport studies. Effects such as thickness-dependent atomic structure and thickness-dependent electron transport may therefore begin to play a role. As a result, the analysis of spin transport for these materials needs to be adjusted to include such effects.

In this work, we study spin pumping into and spin current transport in tantalum (Ta). Ta is widely used as a seed or adhesion layer for magnetic thin-film structures [23–26]. Ta also has a large spin Hall effect [27,28], allowing the generation of pure spin current by charge current, as well as high resistivity [29,30] and short diffusion length [18]. Despite the wide use of Ta in thin films and magnetic structures, some of its properties remain controversial. For example, values of spin diffusion length range from 1.2 nm [31], 2.5 nm [32], up to 10 nm [33]. Recently, a negative spin mixing conductance $\tilde{g}_{\uparrow\downarrow}$, inferred from spin pumping experiments in Ta by Behera *et al.* [34], adds even more to this controversy.

We report on spin pumping and spin transport studies using magnetic single-layer (SL) and double-layer (DL) heterostructures, where SL = $\mathrm{FM_1}$|NM and DL = $\mathrm{FM_1}$|NM|$\mathrm{FM_2}$. In these studies, $\mathrm{FM_1}$ is 3 nm Py (= $\mathrm{Ni_{80}Fe_{20}}$), NM is Ta, and $\mathrm{FM_2}$ = [Py|Fe] is an effective ferromagnetic layer of direct exchange coupled 1.5 nm Py and 4.5 nm Fe. The choice of $\mathrm{FM_2}$ was such that $\mathrm{FM_1}$ and $\mathrm{FM_2}$ have widely separated resonance fields for a given frequency. This will be shown to be very useful as it allows one to study spin transport in Ta using both spin pump and spin sink effects.

The structure of thin-film Ta (0.4–20 nm) was investigated by x-ray diffraction (XRD) and transmission electron microscopy (TEM). Clear evolution of atomic structure is observed over the full thickness range; Ta initially grows as amorphous or nanocrystalline up to $\sim$2 nm, transitioning through bcc structure and eventually establishing larger, well-defined grains of β-Ta for $d_{\mathrm{Ta}} \gtrsim 10$ nm. Motivated by this, we also performed thickness-dependent resistivity measurements of Ta by the four-point probe technique. This allowed us to extend the analysis of spin diffusion assuming a thickness-dependent resistivity.

*Corresponding author: emontoya@sfu.ca; group website: http://surface-science.phys.sfu.ca

†Corresponding author: ppo@sfu.ca; group website: http://surface-science.phys.sfu.ca

‡Corresponding author: egirt@sfu.ca; group website: http://surface-science.phys.sfu.ca

II. SPIN PUMPING AND SPIN DIFFUSION THEORIES

The transfer of spin momentum from the precessing FM_1 into the NM can be represented as a pure spin current of the form [13,19]

$$\boldsymbol{I}_{\rm sp} = \frac{\hbar}{4\pi}\tilde{g}_{\uparrow\downarrow}\left[\boldsymbol{n}\times\frac{\partial \boldsymbol{n}}{\partial t}\right], \tag{1}$$

where $\boldsymbol{n}(=\boldsymbol{M}/M_{\rm s})$ is the instantaneous direction vector of the magnetization $\boldsymbol{M}$, $\hbar$ is the reduced Planck constant, t is the time, and $\tilde{g}_{\uparrow\downarrow}(\approx 2g_{\uparrow\downarrow})$ is the renormalized spin mixing conductance [19,35].

The spin pumping process leads to a spin accumulation at the interface that can be represented as a nonequilibrium chemical potential imbalance $\Delta\boldsymbol{\mu}$. The spin accumulation at the $FM_1|NM$ interface leads to a backflow spin current given by [19]

$$\boldsymbol{I}_{\rm bf} = -\frac{\tilde{g}_{\uparrow\downarrow}}{4\pi}\boldsymbol{n}\times\Delta\boldsymbol{\mu}\times\boldsymbol{n}\Big|_{x=0}. \tag{2}$$

For small microwave [radio-frequency (rf)] excitation, the induced rf magnetic moment in NM is nearly perpendicular to the saturation magnetic moment in FM_1. Consequently, the rf accumulated spin density is also nearly perpendicular to the saturation magnetization and will be described by $\boldsymbol{\mu}_{\rm s}$, replacing the term $\boldsymbol{n}\times\Delta\boldsymbol{\mu}\times\boldsymbol{n}$ in Eq. (2). The net spin current transmitted across the the $FM_1|NM$ interface is therefore

$$\boldsymbol{I}^{\rm net}_{\rm sp} = \boldsymbol{I}_{\rm sp} + \boldsymbol{I}_{\rm bf}. \tag{3}$$

The spin accumulation then diffuses away from the interface according to the spin diffusion equation

$$i\omega\boldsymbol{\mu}_{\rm s} = D\frac{\partial^2\boldsymbol{\mu}_{\rm s}}{\partial x^2} - \frac{\boldsymbol{\mu}_{\rm s}}{\tau_{\rm sf}}, \tag{4}$$

where ω is the angular frequency of the precessing magnetization of the FM and $\tau_{\rm sf}^{-1}$ is the spin flip scattering rate. $D = v_{\rm F}^2\tau_{\rm el}/3$ is the spin diffusion constant, $v_{\rm F}$ is the Fermi velocity, $\tau_{\rm el}^{-1}$ is the electron momentum scattering rate, all in the NM layer. Since the magnetization precession frequencies are much smaller than the spin flip relaxation rates in these experiments, $\omega \ll \tau_{\rm sf}^{-1}$, the left-hand term in the Eq. (4) approaches zero, $i\omega\boldsymbol{\mu}_{\rm s}\approx 0$.

The general solution of Eq. (4) is of the form

$$\boldsymbol{\mu}_{\rm s}(x) = A\exp\left(\frac{x}{\lambda_{\rm sd}}\right) + B\exp\left(\frac{-x}{\lambda_{\rm sd}}\right), \tag{5}$$

where the coefficients A and B are determined using appropriate boundary conditions given by the magnetoelectronic equations where $\lambda_{\rm sd} = v_{\rm F}\sqrt{\tau_{\rm el}\tau_{\rm sf}/3}$ is the spin diffusion length.

The boundary condition at the $FM_1|NM$ interface ($x=0$) is [13]

$$-D\frac{\partial}{\partial x}\boldsymbol{\mu}_{\rm s}(x) = \frac{2}{\mathcal{N}\hbar}\boldsymbol{I}^{\rm net}_{\rm sp}\Big|_{x=0}, \tag{6}$$

where $\mathcal{N}$ is the single spin density of states in the NM.

For the SL structure, the boundary condition at the NM|vacuum interface ($x = d_{\rm NM}$, where $d_{\rm NM}$ is the thickness of the NM) is [35]

$$-D\frac{\partial}{\partial x}\boldsymbol{\mu}_{\rm s}(x) = 0\Big|_{x=d_{\rm NM}}, \tag{7}$$

representing a reflection of spin current. In the DL structure, when FM_1 and FM_2 have different resonances, FM_2 acts as a spin sink for currents pumped from FM_1. The boundary condition at the $NM|FM_2$ interface is given as [35]

$$-D\frac{\partial}{\partial x}\boldsymbol{\mu}_{\rm s}(x) = \frac{\tilde{g}_{\uparrow\downarrow}}{2\pi\mathcal{N}\hbar}\boldsymbol{\mu}_{\rm s}(x)\Big|_{x=d_{\rm NM}}. \tag{8}$$

The net spin current pumped into the NM is equal to the net spin momentum pumped by the FM_1. Therefore, the spin pumping induced damping in the FM_1 layer is directly proportional to $\boldsymbol{I}^{\rm net}_{\rm sp}$. For ferromagnetic films thicker than the decoherence length but thin enough for uniform moment precession,

$$\left(\frac{\partial \boldsymbol{M}}{\partial t}\right)_{\rm sp} = \alpha_{\rm sp}\left[\boldsymbol{M}\times\frac{\partial \boldsymbol{n}}{\partial t}\right] = \frac{\gamma}{d_{\rm FM}}\left(\boldsymbol{I}_{\rm sp} - \frac{\tilde{g}_{\uparrow\downarrow}}{4\pi}\boldsymbol{\mu}_{\rm s}(0)\right), \tag{9}$$

where $\gamma = g\mu_{\rm B}/\hbar$ is the absolute value of the gyromagnetic ratio, $\mu_{\rm B}$ is the Bohr magneton, and $\alpha_{\rm sp}$ is the increase in Gilbert damping due to spin pumping. The term before the brackets on the right-hand side of Eq. (9) takes into account the conversion from spin dynamics to magnetization dynamics and the fact that, for ultrathin FM_1, the interface transfer of moment is shared equally throughout the volume of FM_1 by the exchange interaction.

By using Eqs. (4)–(7) and (9) the spin pumping induced damping in the FM_1 for the $FM_1|NM$ structure can be determined to be

$$\alpha^{\rm SL}_{\rm sp} = \frac{g\mu_{\rm B}}{4\pi M_{\rm s}}\frac{\tilde{g}_{\uparrow\downarrow}}{d_{\rm FM}}\left[1+\frac{\tilde{g}_{\uparrow\downarrow}\mathcal{R}}{\tanh\left(\frac{d_{\rm NM}}{\lambda_{\rm sd}}\right)}\right]^{-1}, \tag{10}$$

where $\mathcal{R} = \frac{\rho e^2}{2\pi\hbar}\lambda_{\rm sd}$, e is the fundamental charge, and $\rho^{-1} = D\mathcal{N}e^2$ is resistivity determined from the Einstein relation.

Using Eqs. (4)–(6) and (8) and (9), one finds in the $FM_1|NM|FM_2$ structure

$$\alpha^{\rm DL}_{\rm sp} = \frac{g\mu_{\rm B}}{4\pi M_{\rm s}}\frac{\tilde{g}_{\uparrow\downarrow}}{d_{\rm FM}}\left[1+\tilde{g}_{\uparrow\downarrow}\mathcal{R}\left(\frac{1+\tilde{g}_{\uparrow\downarrow}\mathcal{R}\tanh\left(\frac{d_{\rm NM}}{\lambda_{\rm sd}}\right)}{\tanh\left(\frac{d_{\rm NM}}{\lambda_{\rm sd}}\right)+\tilde{g}_{\uparrow\downarrow}\mathcal{R}}\right)\right]^{-1}. \tag{11}$$

III. SAMPLE PREPARATION

Radio-frequency (rf) magnetron sputtering was used to deposit Ta(3)|Py(3.5)|Ta($d_{\rm Ta}$)|Au(3.6) and Ta(3)|Py(3.5)|Ta($d_{\rm Ta}$)|Py(1.5)|Fe(4.5)|Au(3.6) films at room temperature on oxidized Si, where the numbers in parentheses indicate the layer thicknesses in nm. A 3-nm-thick Ta seed layer was used to establish the [111] growth orientation of Py. The thickness of the Ta overlayer was varied, with $d_{\rm Ta} =$ 0, 0.3, 0.6, 0.8, 1.2, 2.0, 3.1, and 10.0 nm. A thin gold capping layer was used to protect from formation of oxide. Additionally, Ta films were deposited on glass substrates for use in resistivity measurements. Layer thicknesses were inferred from fitting x-ray reflectivity measurements, allowing for a calibration of the growth rates.

Sputter deposition was performed at an argon pressure of 1.5×10^{-3} Torr. The base pressure of the system was below 5×10^{-8} Torr. Before deposition, the substrates were cleaned with acetone and isopropyl alcohol under ultrasonic conditions at 333 K. RCA cleaning was used to remove oxide residues from Si(100) wafers. In RCA cleaning, Si substrates are soaked for ~15 min in a solution of deionized (DI) water, NH_4OH and H_2O_2, that is kept at $343 + / - 5$ K. After the cleaning, the Si substrates are rinsed with DI water.

IV. EXPERIMENTAL DETAILS

A. Resistivity

Ex situ resistivity measurements were done on sputter-grown glass|Ta(d_{Ta}), for $1 < d_{\mathrm{Ta}} < 23$ nm. Naturally formed surface oxide (≈ 2 nm) is expected to have negligible contribution to the resistivity due the oxide layer and Ta being in parallel with respect to the resistivity measurement.

Collinear four-point probe measurements were made along the symmetry axis on a 12×12 mm sample. The resistances $R_A = V_{23}/I_{14}$, $R_B = V_{24}/I_{13}$, and $R_C = V_{43}/I_{12}$ were measured by means of an ac resistance bridge. The subscripts on I and V indicate the probes where current is supplied and voltage is measured (see inset in Fig. 1); for example, for R_A an ac current I is supplied between points 1 and 4 and the voltage is measured at points 2 and 3. R_A, R_B, and R_C must satisfy the following two relations [36]:

$$\exp\left(-\frac{2\pi R_A d}{\rho}\right) + \exp\left(-\frac{2\pi R_C d}{\rho}\right) = 1 \qquad (12)$$

and

$$\exp\left(\frac{2\pi R_A d}{\rho}\right) - \exp\left(\frac{2\pi R_B d}{\rho}\right) = 1, \qquad (13)$$

where ρ is the resistivity and d is the thickness of the film. In practice, small deviations in probe spacing are corrected by averaging a symmetric measurement for the R's, for example, $R_A = (V_{23}/I_{14} + V_{14}/I_{23})/2$.

Due to limitations of the measurement, the thinnest measured Ta sample was 1.0 nm. A fit was done to extrapolate/interpolate for any $\rho(d_{\mathrm{Ta}})$ required for the α_{sp} analysis. The fitting model does not include the effects of an evolving atomic structure, amorphous/nanocrystalline $\Rightarrow$ bcc $\Rightarrow$ β,

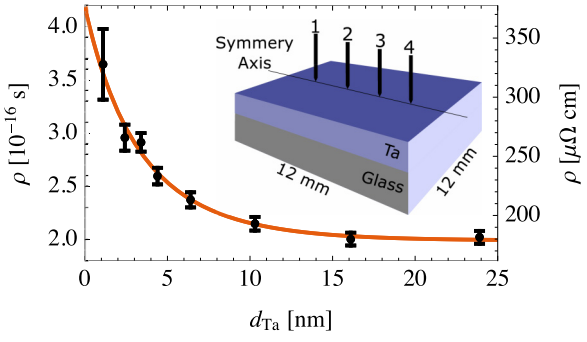

FIG. 1. Resistivity as a function of Ta film thickness grown on glass substrate. The inset shows the geometry and labeling scheme for the four-point probe measurements.

or the increase of grain size with film thickness. The authors of this work are not aware of a model that encompasses all these features in a meaningful way. As a result, we decided on a variation of the commonly used Fuchs-Sondheimer [37,38] model, which includes scattering from both film surfaces and grain boundaries [39]

$$\rho = \rho_\infty \left[1 - \left(\frac{1}{2} + \frac{3}{4}\frac{\lambda_m}{d_{\mathrm{Ta}}}\right)(1 - e^{-\zeta d_{\mathrm{Ta}}/\lambda_m})e^{-d_{\mathrm{Ta}}/\lambda_m}\right]^{-1}, \qquad (14)$$

where $\lambda_m = v_{\mathrm{F}}\tau_{\mathrm{el}}^{\mathrm{bulk}} = 4.7(8)$ nm is the electron mean-free path, $\rho_\infty = 1.99(4) \times 10^{-16}$ s [179(4) $\mu\Omega$ cm] is the bulk resistivity, $\zeta = 0.70(7)$ is a parameter governed by the number of electrons scattered by the grain boundaries. The bulk resistivity approaches the values for β-Ta reported in literature, $\rho_{\beta\text{-Ta}} = 1.9$–$2.4 \times 10^{-16}$ s [170–220 $\mu\Omega$ cm] [29]. The inferred mean-free path λ_m is an order of magnitude higher than the reported values for β-Ta, 0.3–0.5 nm [32,40]. However, from XRD it is observed that for $3 < d_{\mathrm{Ta}} < 10$ nm, the only observed crystal structure is bcc-Ta; the mean-free path for bcc-Ta is an order of magnitude larger than for β-Ta [41].

B. X-ray diffraction

Out-of-plane x-ray diffraction (XRD) measurements using CuK_α radiation were performed on glass|Ta(d_{Ta}) and Si|Ta(3)|Py(3.5)|Ta(20.1)|Au(3.6) films structures [see Figs. 2(a) and 2(b)]. Additionally, in-plane XRD was performed on glass|Ta(d_{Ta}) at a grazing incidence angle of 0.5° [see Fig. 2(c)]. For the in-plane XRD measurements, the incident and scattered beams are nearly parallel to sample surface, allowing for the measurement of lattice planes nearly perpendicular to the sample surface. The low incident angle results in a smaller penetration depth and higher surface structure sensitivity; this technique is advantageous for thin-film and surface measurements.

In Fig. 2(c), a *weak* signal appears in the data at $d_{\mathrm{Ta}} = 3$ nm, near the expected (110) bcc-Ta position. This signal evolves with increasing thickness, and by 6 nm a clear crystalline bcc-Ta peak is observed. With the out-of-plane XRD measurements in Fig. 2(b) we see clear signs of β-Ta by $d_{\mathrm{Ta}} \approx 16$ nm. Both Py and Au grow along the [111] direction when grown on Ta.

C. Transmission electron microscopy

Transmission electron microscopy (TEM) analysis of a Si|Ta(3)|Py(3.5)|Ta(20)|Au(3.6) cross section was performed using an image C_s-corrected Titan 80-300 microscope (FEI) operated at an accelerating voltage of 300 kV. A bright-field TEM overview image of the layer structure is shown in Fig. 2(d), while a corresponding high-resolution TEM (HRTEM) micrograph is presented below it. As can be seen in Fig. 2(e), there is a thin silicon oxide layer between the Si substrate and the Ta(3) layer. Based on the uniform gray level in Fig. 2(d) and the absence of lattice fringes in Fig. 2(e), the Ta(3) layer seems to be characterized by an amorphous structure, whereas the overlying Py(3.5) layer is crystalline. Ta deposited on Py initially grows lacking long-range order. However, we cannot conclude unequivocally whether this

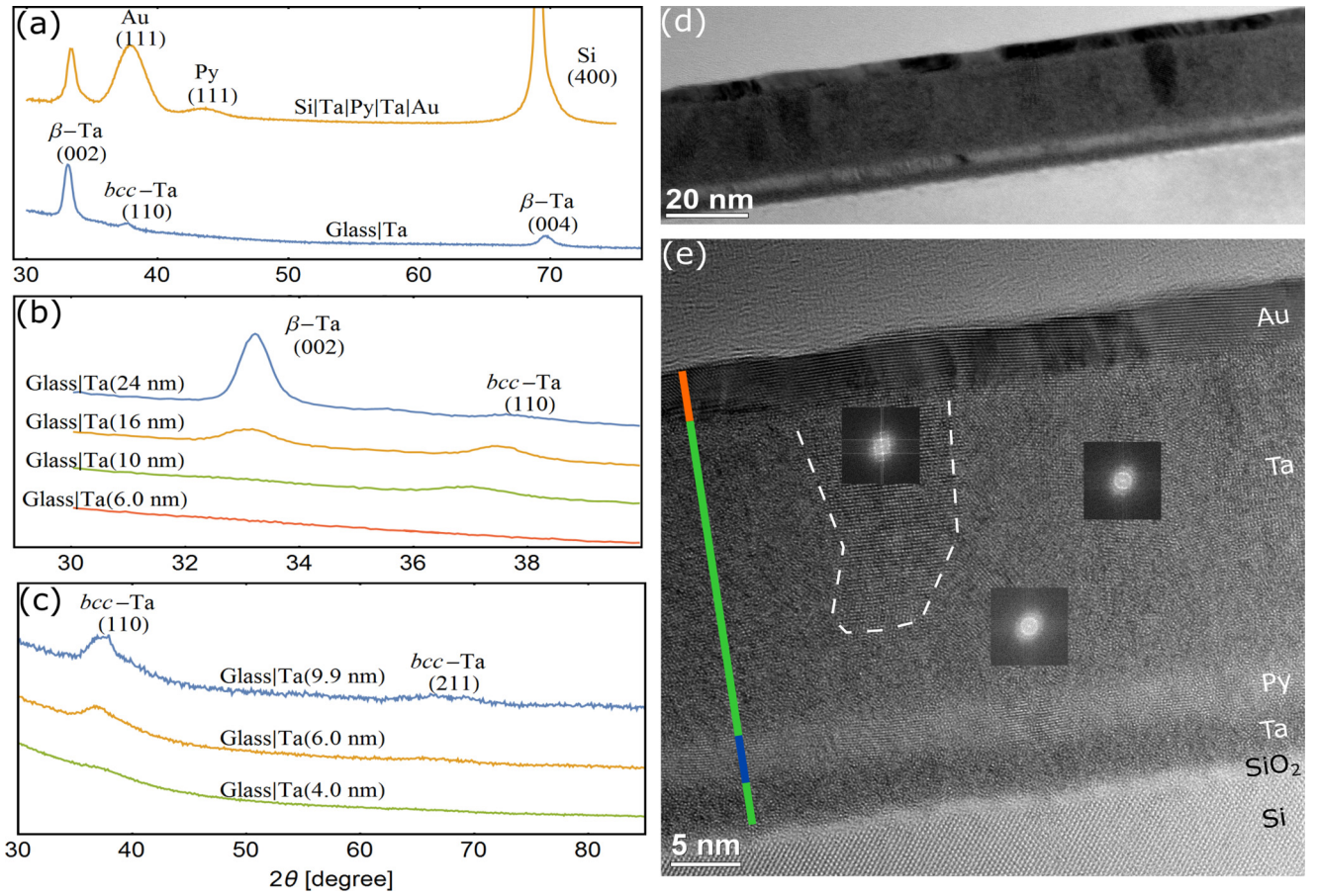

FIG. 2. Out-of-plane θ-2θ XRD scan of (a) Si|Ta(3)|Py(3.5)|Ta(20.1)|Au(3.6), glass|Ta(20.1) and of (b) glass|Ta(d_{Ta}). (c) In-plane XRD scan at a 0.5° grazing incidence angle of glass|Ta(d_{Ta}). (d) Cross-sectional bright-field TEM and (e) HRTEM micrographs of the Si|Ta(3)|Py(3.5)|Ta(20)|Au(3.6) structure. The FFTs of three different regions in the Ta(20) layer are displayed in the corresponding square insets. A dashed white line is drawn around the β-Ta grain to outline its edges.

region is amorphous or partially nanocrystalline with a grain size of 1–2 nm, and therefore we will refer to it as the *intermediate*-Ta region. As the film thickness is increased, larger β-Ta grains are formed, as confirmed by fast Fourier transform (FFT) analysis of the HRTEM image in Fig. 2(e). In particular, the FFT calculated from the grain marked with a dashed white line is best described by a [210] zone axis pattern of β-Ta, where the (002) lattice planes are parallel to the sample surface. It should be mentioned that diffractograms obtained from other parts of the Ta(20) layer in Fig. 2(e) cannot be indexed unambiguously. In conclusion, the TEM findings are consistent with the observations from XRD. Furthermore, the in-plane XRD suggests that some of the nanocrystals in the thin limit ($\lesssim$ 10 nm) are bcc-Ta, which get overshadowed by large grain β-Ta for the thicker films.

The large difference in resistivity of amorphous-Ta $\sim$3.0–22 $\times$ 10^{-16} s, bcc-Ta $\sim$ 0.33 $\times$ 10^{-16} s, and β-Ta $\sim$ 2.2 $\times$ 10^{-16} s [30,42] implies that the evolution of Ta structure with thickness can contribute to the thickness-dependent Ta resistivity shown in Fig. 1.

D. Ferromagnetic resonance

The Landau-Lifshitz-Gilbert equation describes the magnetization dynamics in the ferromagnetic resonance (FMR) experiment,

$$\frac{\partial \boldsymbol{M}}{\partial t} = -\gamma[\boldsymbol{M} \times \boldsymbol{H}_{\mathrm{eff}}] + \alpha\left[\boldsymbol{M} \times \frac{\partial \boldsymbol{n}}{\partial t}\right], \tag{15}$$

where $\boldsymbol{M}$ is the instantaneous magnetization vector with magnitude M_{s}, $\boldsymbol{n}$ is the unit vector parallel to $\boldsymbol{M}$, $\boldsymbol{H}_{\mathrm{eff}}$ is the sum of internal and external H fields, and α is the dimensionless Gilbert damping parameter.

FMR measurements were carried out at room temperature on coplanar waveguide in an in-plane field-swept, field-modulated configuration, as detailed in Ref. [43] over a frequency range of 6–36 GHz. The measured FMR data were described by an admixture of the χ' and χ'' components of the complex transverse magnetic susceptibility $\chi = \chi' + i\chi''$. The FMR data were fit as described by Refs. [43,44]. Interlayer exchange coupling was not observed for the DL structure for $d_{\mathrm{Ta}} \geqslant 0.6$ nm. $M_{\mathrm{s}} = 806 \pm 4$ emu/cm^3 was determined independently by means of superconducting quantum interference device (SQUID) magnetometry measurements on three reference samples of Ta(3)|Py(3.5)|Au(3.6).

The samples studied were polycrystalline and showed no in-plane anisotropy. The resonance condition was

$$\left(\frac{\omega}{\gamma}\right)^2 = (H_{\mathrm{FMR}})(H_{\mathrm{FMR}} + 4\pi M_{\mathrm{eff}}), \tag{16}$$

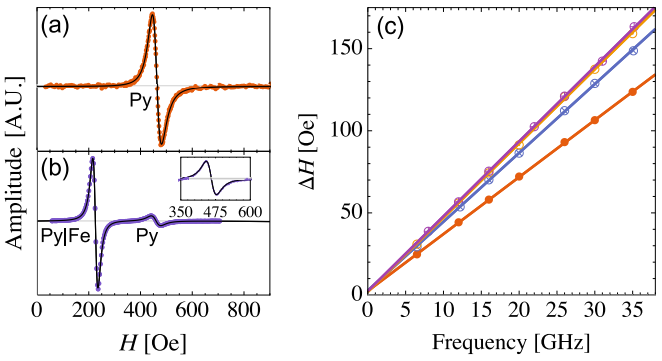

FIG. 3. Example 6.5-GHz FMR spectra for (a) SL ($FM_1 = Py$) and (b) DL ($FM_1 = Py$, $FM_2 = Py|Fe$) samples with $d_{Ta} = 1.0$ nm. Inset of (b) is an expanded view of the $FM_1 = Py$ resonance line. (c) FMR linewidth as a function of frequency. SL samples with $d_{Ta} =$ (●) 0 nm (⊗) 0.8 nm, and (⊙) 10 nm with $\alpha = 10.2$, 12.4, and 13.3 $\times 10^{-3}$, respectively. DL sample with $d_{Ta} =$ (⊕) 0.8 nm and $\alpha = 13.2 \times 10^{-3}$.

where H_{FMR} is the resonance field, $4\pi M_{eff} = 4\pi M_s - 2K_U^{\perp}/M_s$, and $K_U^{\perp}$ is the perpendicular-to-film-plane uniaxial anisotropy. The Landé g factor for all samples was determined, by fitting the frequency dependence of H_{FMR} using Eq. (16), to be $g = 2.10(\pm 0.01)$. This value is in agreement with the g factor of Py measured by various techniques such as FMR [45–47] and time-domain pulsed inductive microwave magnetometry (PIMM) [48,49] and is consistent with Einstein–de Haas [50,51] effect measurements.

The FMR linewidth was well described by Gilbert-type damping

$$\Delta H(\omega) = \alpha \frac{\omega}{\gamma} + \Delta H(0), \tag{17}$$

where ω is the microwave angular frequency, and $\Delta H(0)$ is the zero-frequency line broadening due to long-range magnetic inhomogeneity [52,53]. All of the samples had small zero-frequency offsets, $\Delta H(0) < 3$ Oe, indicating a high level of sample quality and the absence of two-magnon scattering contributions to the damping (see Fig. 3).

V. RESULTS AND DISCUSSION

In the SL and DL structures, there are three main contributions to the damping in the Py(= FM_1) layer: (1) the bulk damping of the Py layer α_{bulk}; (2) the spin-pumping-induced damping due to the Ta(3) seed layer $\alpha_{sp,seed}$ (the Ta seed layer is required to obtain high texturing of Py); (3) the damping due to spin pumping into the Ta(d_{Ta}) overlayer α_{sp}. The total damping is therefore

$$\alpha = \alpha_{bulk} + \alpha_{sp,seed} + \alpha_{sp}. \tag{18}$$

As the Py layer and Ta seed layer are held constant in thickness, the contribution to the total damping

$$\alpha_{ref} = \alpha_{bulk} + \alpha_{sp,seed} \tag{19}$$

itself should remain constant. $\alpha_{ref} = 10.4(\pm 0.2) \times 10^{-3}$ was determined by measuring FMR on five samples of Ta(3)|Py(3.5)|Au(3.6), where the Au capping layer was sufficiently thin not to contribute to spin-pumping-induced damping [54].

The role of Ta in the propagation of pure spin current was investigated by monitoring α_{sp} in both the SL and DL structures as a function of d_{Ta}, where

$$\alpha_{sp} = \alpha - \alpha_{ref}. \tag{20}$$

The d_{Ta} dependence on α_{sp} of the Py(= FM_1) layer in the structures, along with the fitting models, is shown in Fig. 4. With d_{Py} and d_{Ta} determined from low-angle x-ray calibrations, g determined by FMR measurements, M_s determined by SQUID measurements, and ρ determined by four-point probe resistivity measurements, the only free parameters left in Eqs. (10) and (11) are $\tilde{g}_{\uparrow\downarrow}$ and λ_{sd}.

The dependence $\alpha_{sp}(d_{Ta})$ of the SLs and DLs was simultaneously fit using Eqs. (10) and (11), respectively. Different models were used with respect to the choices of the parameters λ_{sd} and ρ.

(1) $\tilde{g}_{\uparrow\downarrow}$, ρ, *and* λ_{sd} *are free parameters*. This model fits for an average ρ and λ_{sd} and is mostly sensitive to the d_{Ta} range where α_{sp} is changing.

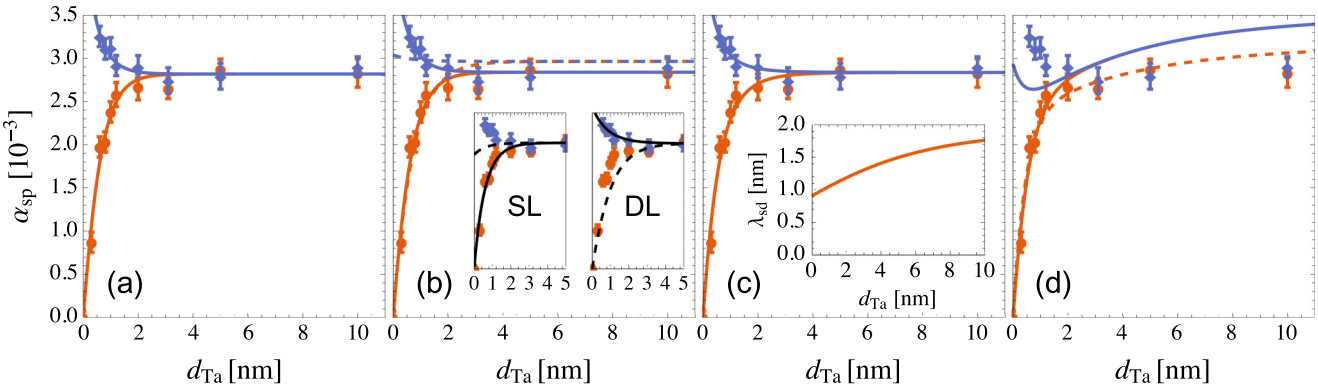

FIG. 4. Damping due to spin pumping into the Ta overlayer as a function of d_{Ta} for SL (●) and DL (♦) samples. (a) Simultaneous fits using model 1. (b) Main: dashed and solid lines are simultaneous fits using models 2a and 2b, respectively. Inset: individual fits for the SL and DL are shown as solid lines on the left and right panels, respectively. The dashed lines are plots of the complementary data set using the individual fit parameters. (c) Main: simultaneous fit using model 3. Inset: $\lambda_{sd}(d_{Ta})$. (d) The solid lines are simultaneous fit while the dashed line is a fit to only the SL data.

(2) *$\tilde{g}_{\uparrow\downarrow}$ and λ_{sd} are free parameters, while, a constant ρ is taken from resistivity measurements.* Taking the bulklike ρ is the most common approach usually found in literature.

(3) *$\tilde{g}_{\uparrow\downarrow}$ is a free parameter, $\rho(d_{Ta})$ is taken from resistivity measurements, and λ_{sd} is fitting parameter restricted to be inversely proportional to $\rho(d_{Ta})$.*

(4) *$\tilde{g}_{\uparrow\downarrow}$ is a free parameter, $\rho(d_{Ta})$ is taken from resistivity measurements, and λ_{sd} is thickness-independent fitting parameter.* This model was recently proposed in Ref. [55].

Model 1 describes both the SL and DL data well [see solid lines in Fig. 4(a)]. The fit parameters are $\tilde{g}_{\uparrow\downarrow} = 1.7(3) \times 10^{15}$ cm^{-2}, $\lambda_{sd} = 1.0(1)$ nm, $\rho = 4.1(6) \times 10^{-16}$ s [360(50) $\mu\Omega$ cm]. The value of ρ from this fit is consistent with the resistivity measured in the Ta film in the *intermediate*-Ta region.

Model 2 can be interpreted in two logical limits: (a) using the bulk resistivity ($\rho_\infty = 1.99 \times 10^{-16}$ s) and (b) using the ρ value measured in the region where spin currents are being absorbed. A simultaneous fit with model 2a shows that the SL data can be qualitatively described by this model while the DL data cannot [see dashed lines in Fig. 4(b)]. The SL and DL data sets can be fit individually with model 2a [see inset in Fig. 4(b)], but yield disagreeing fit parameters (see Table I). In model 2b, one can use $\rho = 3.6 \times 10^{-16}$ s for the $d_{Ta} = 1.1$ nm sample. The motivation is that the region where α_{sp} shows a large dependence on d_{Ta}, i.e., where there is significant spin transport, is the *intermediate*-Ta region, where four-point probe measurement showed the large resistivity. This model describes both the SL and DL data well, and the individual and simultaneous fits agree within error as shown in Table I. The simultaneous fit is shown by the solid lines in Fig. 4(b). The simultaneous fit parameters are $\tilde{g}_{\uparrow\downarrow} = 1.53 \times 10^{15}(8)$ cm^{-2} and $\lambda_{sd} = 1.03(3)$ nm. These values are consistent with model 1.

Model 3 is akin to the Elliot-Yafet mechanism [56,57]. In this model $\tau_{sf} \propto \tau_{el}$, as parametrized by ρ, includes all electron scattering events as opposed to only scattering in the bulk. The thickness dependence of the spin diffusion length was taken to be

$$\lambda_{sd}(d_{Ta}) = \lambda_{sd}^{bulk} \frac{\rho_\infty}{\rho(d_{Ta})}, \tag{21}$$

TABLE I. Spin diffusion model fit parameters. SL and DL refer to individual fits of the magnetic single-layer and double-layer data, respectively, otherwise fits are a simultaneous fit to both data sets shown in Fig. 4.

Model	$\tilde{g}_{\uparrow\downarrow}$ (10^{15} cm^{-2})	λ_{sd} (nm)	ρ (10^{-16} s)
1	1.7(3)	1.0 (1)	4.1(6)
2a	1.09(4)	1.39 (4)	1.99
2a (SL)	0.92(6)	1.27 (6)	1.99
2a (DL)	1.31(6)	1.7 (1)	1.99
2b	1.53(8)	1.03 (3)	3.6
2b (SL)	1.4(2)	1.00 (5)	3.6
2b (DL)	1.6(1)	1.03 (6)	3.6
3	1.57(8)	1.91 (5)	$\rho(d_{Ta})$
3 (SL)	1.6(2)	1.90 (8)	$\rho(d_{Ta})$
3 (DL)	1.6(1)	1.9 (1)	$\rho(d_{Ta})$
4 (SL)	0.9 (5)	0.86 (4)	$\rho(d_{Ta})$

where λ_{sd}^{bulk} is the thick-film limit of the spin diffusion length. The fitted parameters are $\tilde{g}_{\uparrow\downarrow} = 1.57(8) \times 10^{15}$ cm^{-2} and $\lambda_{sd}^{bulk} = 1.91(5)$ nm. This model also describes both the SL and DL data well in both individual and simultaneous fits (see Table I). The simultaneous fit is shown by the solid lines in Fig. 4(c). $\lambda_{sd}(d_{Ta})$ is plotted in the inset of Fig. 4(c). The fit value of the spin mixing conductance is in good agreement with both models 1 and 2(b), however, λ_{sd}^{bulk} is nearly twice as large as λ_{sd} in models 1 and 2(b).

Model 4 was recently proposed in Ref. [55] and described well the spin pumping experiments in the following SL heterostructures: Ta|Py|Pt, Ta|Py|Cu|Pt, Ta|Py|Pd, and Ta|Py|Cu|Pd. The model is equivalent to having $\tau_{sf} \propto 1/\tau_{el}$. We are unable to simultaneously fit the SL and DL data with this model [see solid lines in Fig. 4(d)]. This model is able to describe, within the measurement errors, the SL data only, as shown by the dashed line in Fig. 4(d). The DL data cannot be described by this model, attempts to fit the DL results in a curve similar to the blue (top) fit in Fig. 4(d).

It is worth comparing the models that give good fits. In model 1, one is essentially fitting for both an average λ_{sd} and ρ in the region where α_{sp} is changing. The best fit ρ from model 1 agrees well with the ρ measured by four-point probe in the thickness range where α_{sp} has large dependence on d_{Ta}, so it is not surprising that models 1 and 2b give fit values for λ_{sd} and $\tilde{g}_{\uparrow\downarrow}$ that agree within measurement error. Model 3 yields a $\tilde{g}_{\uparrow\downarrow}$ value that is consistent with models 1 and 2b. While the λ_{sd}^{bulk} is nearly twice the value of λ_{sd} in the aforementioned models, the average spin diffusion length in the first 3 nm of Ta is $\lambda_{sd}^{ave} \simeq 1.1$ nm. In this regime, model 3 is in agreement with models 1 and 2b. This indicates that λ_{sd}^{bulk}, as an extrapolated parameter, should not be taken to have much physical significance. Models 1 and 2b can be seen as the same as model 3 with different approaches to averaging the electron transport properties in this thickness regime.

Models 2a and 4 cannot describe the SL and DL data simultaneously, but both can be used to describe the SL data. While model 2a can fit SL and DL separately, fitting the single-layer data with model 2a requires less efficient spin pumping (smaller $\tilde{g}_{\uparrow\downarrow}$) and more efficient spin absorption in Ta (smaller λ_{sd}) than fitting the DL data. Using the SL fit parameters to calculate DL [Eq. (11)], model 2a yields an increase of α_{sp} with increasing Ta thickness, indicating that Ta is a more efficient spin absorber than spin sink. In other words, this model requires that spin absorption is occurring faster than in the diffusive limit, which is a mathematically achievable dependence that lacks physical significance. Using the DL fit parameters in the SL model underestimates the the damping in the first 2 nm of Ta [see inset in Fig. 4(b)]. The simultaneous fit is an average of these limits, which leads the nearly flat dependence of the DL. Model 4 fails for the DL for a similar reason. Additionally, none of the tested models result in a negative spin conductance, such as the one reported in Ref. [34].

VI. CONCLUSIONS

Spin pumping and spin transport were studied in magnetic single-layer (SL = Py|Ta) and magnetic double-layer (DL = Py|Ta|[Py|Fe]) heterostructures by measuring the

spin-pumping-induced damping in the Py layer as a function of the Ta layer thickness $\alpha_{sp}(d_{Ta})$. It was found that while the bulk-limit resistivity $\rho_\infty = 1.99(4) \times 10^{-16}$ s could be used in the spin diffusion model to describe $\alpha_{sp}(d_{Ta})$ in SL and DL individually, it resulted in inconsistent parameters. A result pointing out the flaw of this approach and also observed in the simultaneous fit to the two data sets.

The reason that ρ_∞ is inconsistent with the data is because structure of Ta in the region of spin pumping is not bulk-Ta. XRD studies confirmed the bulk structure is a combination of β-Ta and bcc-Ta. However, Ta initially grows without long-range order for ~2 nm on the Py layer, which corresponds to the region where spin currents can propagate as indicated by the $\alpha_{sp}(d_{Ta})$ data. Using the resistivity measured in the *intermediate*-Ta region, $\rho = 3.6 \times 10^{-16}$ s, the spin diffusion model can describe $\alpha_{sp}(d_{Ta})$ for both SLs and DLs with the spin mixing conductance $\tilde{g}_{\uparrow\downarrow} = 1.53(8) \times 10^{15}$ cm^{-2} and the spin diffusion length $\lambda_{sd} = 1.0(1)$ nm. Furthermore, allowing ρ to be a free parameter in a simultaneous fit of the SL and DL data results in a resistivity that agrees with that measured in the *intermediate*-Ta region within error $\rho = 4.1(6) \times 10^{-16}$ s as well as agreement in $\tilde{g}_{\uparrow\downarrow}[1.7(3) \times 10^{15}$ cm$^{-2}]$ and $\lambda_{sd}[= 1.03(3)$ nm].

Additionally, $\alpha_{sp}(d_{Ta})$ was modeled taking into account the thickness dependence of the resistivity. A model assuming a thickness-dependent spin diffusion length such that $\lambda_{sd} \propto \rho^{-1}$ (equivalent to $\tau_{sf} \propto \tau_{el}$) could describe both the SL and DL data and resulted in $\tilde{g}_{\uparrow\downarrow} = 1.53(8) \times 10^{15}$ cm^{-2} and $\lambda_{sd}(d_{Ta} = \infty) = 1.91(5)$ nm. The bulklike $\lambda_{sd}(d_{Ta} = \infty)$ obtained in this model is an extrapolated parameter and should not be taken to have physical meaning. However, the average value of λ_{sd} in the *intermediate*-Ta region where spin currents are propagating agrees well with the above (non-bulk-resistivity) models. A model assuming a constant λ_{sd} and thickness dependent ρ (equivalent to $\tau_{sf} \propto 1/\tau_{el}$) could be used to describe the SL data alone, but could not describe the DL data. The resulting spin diffusion parameters for the the SL fit, $\tilde{g}_{\uparrow\downarrow} = 0.9(5) \times 10^{15}$ cm^{-2} and $\lambda_{sd} = 0.86(4)$ nm, did not agree with the other models.

We find that sputter-deposited Ta presents a unique challenge in the study of spin transport, where it is often assumed that the structure of the material is uniform throughout the entire thickness. This is a good approximation for materials with long spin diffusion lengths such as Au, Cu, and Ag. For Ta, however, the structure transitions from lacking long-range order to polycrystalline on a length scale that is of the order of the diffusion length. The result is that bulk resistivity cannot be used in the spin diffusion model to accurately describe the spin transport. This conclusion cannot be reached by analyzing data from only the SL structure; in fact, the SL can always be fit with any of the tested models, yielding diverse parameters. *It is necessary to have both the SL and DL, and to use the spin pump and spin sink effects in order to extract a meaningful spin diffusion length and spin mixing conductance for Ta.* This may be one source of the disagreement in spin diffusion parameters in Ta, as often the structure and resistivity are determined from thicker films, by XRD, and four-probe measurements, respectively.

ACKNOWLEDGMENTS

Financial support from the Natural Sciences and Engineering Research Council of Canada (NSERC) and Canadian Institute for Advanced Research (CIFAR) is gratefully acknowledged. In addition, support by the Structural Characterization Facilities Rossendorf at IBC is gratefully acknowledged.

[1] S. A. Wolf, D. D. Awschalom, R. A. Buhrman, J. M. Daughton, S. von Molnár, M. L. Roukes, A. Y. Chtchelkanova, and D. M. Treger, Science **294**, 1488 (2001).
[2] I. Žutić, J. Fabian, and S. D. Sarma, Rev. Mod. Phys. **76**, 323 (2004).
[3] P. Khalili Amiri, Z. M. Zeng, J. Langer, H. Zhao, G. Rowlands, Y. J. Chen, I. N. Krivorotov, J. P. Wang, H. W. Jiang, J. A. Katine, Y. Huai, K. Galatsis, and K. L. Wang, Appl. Phys. Lett. **98**, 112507 (2011).
[4] S.-Y. Huang, D. Qu, and C.-L. Chien, *Solid State Physics*, Vol. 64 (Elsevier, Amsterdam, 2013), pp. 53–82.
[5] R. Urban, G. Woltersdorf, and B. Heinrich, Phys. Rev. Lett. **87**, 217204 (2001).
[6] S. Mizukami, Y. Ando, and T. Miyazaki, J. Magn. Magn. Mater. **239**, 42 (2002).
[7] B. Heinrich, Y. Tserkovnyak, G. Woltersdorf, A. Brataas, R. Urban, and G. E. W. Bauer, Phys. Rev. Lett. **90**, 187601 (2003).
[8] A. Azevedo, L. H. Vilela-Leão, R. L. Rodríguez-Suárez, A. F. Lacerda Santos, and S. M. Rezende, Phys. Rev. B **83**, 144402 (2011).
[9] C. T. Boone, H. T. Nembach, J. M. Shaw, and T. J. Silva, J. Appl. Phys. **113**, 153906 (2013).
[10] Y. Kitamura, E. Shikoh, Y. Ando, T. Shinjo, and M. Shiraishi, Sci. Rep. **3**, 1739 (2013).
[11] E. Montoya, B. Heinrich, and E. Girt, Phys. Rev. Lett. **113**, 136601 (2014).
[12] C. Du, H. Wang, F. Yang, and P. C. Hammel, Phys. Rev. Appl. **1**, 044004 (2014).
[13] Y. Tserkovnyak, A. Brataas, and G. E. W. Bauer, Phys. Rev. Lett. **88**, 117601 (2002).
[14] E. Šimánek and B. Heinrich, Phys. Rev. B **67**, 144418 (2003).
[15] F. J. Jedema, M. S. Nijboer, A. T. Filip, and B. J. van Wees, Phys. Rev. B **67**, 085319 (2003).
[16] B. Kardasz, O. Mosendz, B. Heinrich, Z. Liu, and M. Freeman, J. Appl. Phys. **103**, 07C509 (2008).
[17] E. Montoya, B. Kardasz, C. Burrowes, W. Huttema, E. Girt, and B. Heinrich, J. Appl. Phys. **111**, 07C512 (2012).
[18] H. L. Wang, C. H. Du, Y. Pu, R. Adur, P. C. Hammel, and F. Y. Yang, Phys. Rev. Lett. **112**, 197201 (2014).
[19] Y. Tserkovnyak, A. Brataas, G. E. W. Bauer, and B. I. Halperin, Rev. Mod. Phys. **77**, 1375 (2005).
[20] J. Foros, G. Woltersdorf, B. Heinrich, and A. Brataas, J. Appl. Phys. **97**, 10A714 (2005).
[21] X. D. Tao, Z. Feng, B. F. Miao, L. Sun, B. You, D. Wu, J. Du, W. Zhang, and H. F. Ding, J. Appl. Phys. **115**, 17C504 (2014).

[22] M. Caminale, A. Ghosh, S. Auffret, U. Ebels, K. Ollefs, F. Wilhelm, A. Rogalev, and W. E. Bailey, Phys. Rev. B **94**, 014414 (2016).
[23] S. N. Piramanayagam, C. S. Mah, C. Y. Ong, J. Z. Shi, J. A. Dumaya, T. Onoue, and S. Ishibashi, J. Appl. Phys. **101**, 103914 (2007).
[24] S. N. Piramanayagam, J. Appl. Phys. **102**, 011301 (2007).
[25] S. Ikeda, K. Miura, H. Yamamoto, K. Mizunuma, H. D. Gan, M. Endo, S. Kanai, J. Hayakawa, F. Matsukura, and H. Ohno, Nat. Mater. **9**, 721 (2010).
[26] S. Mangin, D. Ravelosona, J. A. Katine, M. J. Carey, B. D. Terris, and E. E. Fullerton, Nat. Mater. **5**, 210 (2006).
[27] L. Liu, C.-F. Pai, Y. Li, H. W. Tseng, D. C. Ralph, and R. A. Buhrman, Science **336**, 555 (2012).
[28] S.-I. Kim, D.-J. Kim, M.-S. Seo, B.-G. Park, and S.-Y. Park, Appl. Phys. Lett. **106**, 032409 (2015).
[29] N. O. Nnolim, T. A. Tyson, and L. Axe, J. Appl. Phys. **93**, 4543 (2003).
[30] K. Stella, D. Bürstel, S. Franzka, O. Posth, and D. Diesing, J. Phys. D: Appl. Phys. **42**, 135417 (2009).
[31] J. H. Kwon, P. Deorani, J. Yoon, M. Hayashi, and H. Yang, Appl. Phys. Lett. **107**, 022401 (2015).
[32] G. Allen, S. Manipatruni, D. E. Nikonov, M. Doczy, and I. A. Young, Phys. Rev. B **91**, 144412 (2015).
[33] O. Boulle, V. Cros, J. Grollier, L. G. Pereira, C. Deranlot, F. Petroff, G. Faini, J. Barnaś, and A. Fert, Nat. Phys. **3**, 492 (2007).
[34] N. Behera, S. Chaudhary, and D. K. Pandya, Sci. Rep. **6**, 19488 (2016).
[35] Y. Tserkovnyak, A. Brataas, and G. E. W. Bauer, Phys. Rev. B **66**, 224403 (2002).
[36] S. Thorsteinsson, F. Wang, D. H. Petersen, T. M. Hansen, D. Kjær, R. Lin, J.-Y. Kim, P. F. Nielsen, and O. Hansen, Rev. Sci. Instrum. **80**, 053902 (2009).
[37] K. Fuchs, Math. Proc. Cambridge Philos. Soc. **34**, 100 (1938).
[38] E. H. Sondheimer, Adv. Phys. **1**, 1 (1952).
[39] P. Fan, K. Yi, J.-D. Shao, and Z.-X. Fan, J. Appl. Phys. **95**, 2527 (2004).
[40] N. O. Nnolim, Understanding the origins of metastability in thin film growth; tantalum and the early group VB-VIB metals, Dissertation, The New Jersey Institute of Technology, 2003.
[41] J. E. Nestell, J. Appl. Phys. **53**, 8993 (1982).
[42] J. Narayan, V. Bhosle, A. Tiwari, A. Gupta, P. Kumar, and R. Wu, J. Vac. Sci. Technol. A **24**, 1948 (2006).
[43] E. Montoya, T. McKinnon, A. Zamani, E. Girt, and B. Heinrich, J. Magn. Magn. Mater. **356**, 12 (2014).
[44] E. Montoya, T. Sebastian, H. Schultheiss, B. Heinrich, R. E. Camley, and Z. Celinski, in *Magnetism of Surfaces, Interfaces, and Nanoscale Materials*, 1st ed., Vol. 5, edited by R. E. Camley, Z. Celinski, and R. L. Stamps (Elsevier, Amsterdam, 2016), Chap. 3, pp. 113–167.
[45] D. Bastian and E. Biller, Phys. Status Solidi A **35**, 465 (1976).
[46] J. M. Shaw, H. T. Nembach, and T. J. Silva, Appl. Phys. Lett. **99**, 012503 (2011).
[47] J. M. Shaw, H. T. Nembach, T. J. Silva, and C. T. Boone, J. Appl. Phys. **114**, 243906 (2013).
[48] J. P. Nibarger, R. Lopusnik, Z. Celinski, and T. J. Silva, Appl. Phys. Lett. **83**, 93 (2003).
[49] L. Cheng, H. Song, and W. Bailey, IEEE Trans. Magn. **40**, 2350 (2004).
[50] S. J. Barnett and L. A. Giambomi, Phys. Rev. **88**, 28 (1952).
[51] T. M. Wallis, J. Moreland, and P. Kabos, Appl. Phys. Lett. **89**, 122502 (2006).
[52] B. Heinrich and J. Cochran, Adv. Phys. **42**, 523 (1993).
[53] B. Heinrich, in *Ultrathin Magnetic Structures*, Vol. III, edited by J. A. C. Bland and B. Heinrich (Springer, Berlin, 2005), Chap. 5, pp. 143–206.
[54] O. Mosendz, G. Woltersdorf, B. Kardasz, B. Heinrich, and C. H. Back, Phys. Rev. B **79**, 224412 (2009).
[55] C. T. Boone, J. M. Shaw, H. T. Nembach, and T. J. Silva, J. Appl. Phys. **117**, 223910 (2015).
[56] Y. Yafet, Phys. Rev. **85**, 478 (1952).
[57] R. Elliott, Phys. Rev. **96**, 266 (1954).